

# Deep Calibration and Operator Learning for Ground Penetrating Radar Imaging

Shastri, Saurav; Ma, Yanting; Boufounos, Petros T.; Mansour, Hassan

TR2024-128 September 13, 2024

## Abstract

The accurate imaging of underground scenes using wave-based sensor technologies, such as ground penetrating radar, presents challenges due to ill-posedness, formulation complexities, and computational demands. In this paper, we propose a machine learning-based approach that leverages a learned forward model to simulate wave-object interactions inspired by physics principles as well as the calibration to realistic antenna configurations. Our approach combines a learned wave propagation model, referred to as Born FNO, with a deep calibration network that maps a point-receiver scattered wavefields to the response of a desired receiving antenna architecture. We evaluate our method on a simulated dataset that includes multiple ground layers and complex target structures. We demonstrate that our proposed calibration network enables the reconstruction of permittivity distributions and outperforms a linear calibration operator trained on the same dataset by over 4.5 dB in peak signal-to-noise ratio.

*European Signal Processing Conference (EUSIPCO) 2024*

© 2024 MERL. This work may not be copied or reproduced in whole or in part for any commercial purpose. Permission to copy in whole or in part without payment of fee is granted for nonprofit educational and research purposes provided that all such whole or partial copies include the following: a notice that such copying is by permission of Mitsubishi Electric Research Laboratories, Inc.; an acknowledgment of the authors and individual contributions to the work; and all applicable portions of the copyright notice. Copying, reproduction, or republishing for any other purpose shall require a license with payment of fee to Mitsubishi Electric Research Laboratories, Inc. All rights reserved.



# Deep Calibration and Operator Learning for Ground Penetrating Radar Imaging

Saurav K. Shastri<sup>1</sup>, Yanting Ma<sup>2</sup>, Petros Boufounos<sup>2</sup>, Hassan Mansour<sup>2</sup>

<sup>1</sup>Dept. ECE, The Ohio State University, Columbus, OH 43210, USA

<sup>2</sup>Mitsubishi Electric Research Laboratories, 201 Broadway, Cambridge, MA 02140, USA  
shastri.19@osu.edu, {yma, petrosb, mansour}@merl.com

**Abstract**—The accurate imaging of underground scenes using wave-based sensor technologies, such as ground penetrating radar, presents challenges due to ill-posedness, formulation complexities, and computational demands. In this paper, we propose a machine learning-based approach that leverages a learned forward model to simulate wave-object interactions inspired by physics principles as well as the calibration to realistic antenna configurations. Our approach combines a learned wave propagation model, referred to as Born FNO, with a deep calibration network that maps a point-receiver scattered wavefields to the response of a desired receiving antenna architecture. We evaluate our method on a simulated dataset that includes multiple ground layers and complex target structures. We demonstrate that our proposed calibration network enables the reconstruction of permittivity distributions and outperforms a linear calibration operator trained on the same dataset by over 4.5 dB in peak signal-to-noise ratio.

**Index Terms**—Underground Imaging, Diffraction Tomography, Full Waveform Inversion

## I. INTRODUCTION

Ground Penetrating Radar (GPR) offers a non-destructive approach to mapping underground utilities. The process of acquiring radar data includes sending electromagnetic waves below the surface using transmission antennas positioned above the ground. Subsequently, the scattered waves are recorded by receiver antennas, also placed above the ground. Utilizing the received scattered waves, data processing is employed to yield insights into the physical characteristics of the subsurface.

Conventional GPR data processing primarily relies on migration methods, which have roots in seismic imaging techniques [1]–[3]. While these methods are efficient and can be implemented in real-time, the images they generate only offer information about the locations and rough shapes of subsurface objects, lacking quantitative details about the dielectric permittivity contrast that could provide insights into the materials present. More advanced data processing approaches, based on inverse scattering [3, 4], aim to estimate the spatial distribution of dielectric permittivity contrast in the subsurface, resulting in more informative images compared to migration methods.

Assuming time harmonic waves, the nonlinear relationship governing the interaction between waves and objects due to multiple scattering can be fully described by an integral equation, with the 2D scalar field setup coinciding with the well-known Lippmann-Schwinger equation [5]. Inverse scattering

based on this integral equation necessitates knowledge of the background medium and efficient methods to compute the corresponding Green’s function. Existing research [6, 7] often considers a homogeneous background, where computing the Green’s function is straightforward. Other studies for the GPR setup have explored layered backgrounds and proposed methods for computing the corresponding Green’s function [3, 8]. While the integral equation formulation is exact, solving it can be computationally expensive, especially when accurate optimization schemes are employed to address the inverse problem [6, 9, 10]. A commonly utilized approximation to the integral equation is based on the Born series expansion, known as the iterative Born approximation (IBA) [4, 11]. Retaining higher-order terms in this series preserves some level of system nonlinearity, resulting in a more accurate approximation.

With the emergence of machine learning-based techniques, recent studies employed architectures like Graph Neural Networks or Fourier Neural Operator (FNO) to characterize the time-domain wave propagation [12, 13]. However, a primary obstacle with these learned solutions is the challenge of accumulating errors during the temporal unrolling process. In our previous work [14], we introduced a network structure, called Born FNO (BFNO)<sup>1</sup>, that is inspired by the iterative Born approximation and adapts the FNO to directly acquire knowledge of the wave-matter interaction in the frequency domain, eliminating the need for prior information about the background medium.

The main bottleneck to applying the above techniques to real GPR settings is the mismatch in the estimation of the forward model describing the GPR antenna system. While analytical (e.g. Lippmann Schwinger) and learned (e.g. FNO, BFNO) techniques are highly effective for dipole antenna systems, real GPR systems exhibit multiple reflections between the antenna and the ground surface as well as frequency dependent electrical properties due to the antenna shape [15]. Moreover, experimental radar systems measure the electric field in 3D whereas the desired computational domain is 2D. The conversion from 3D wavefield measurement to 2D computational domain is a common computation reduction technique in the field of seismic full waveform inversion [16]–[19]. However, these techniques continue to suffer from inaccuracies due to inexact knowledge of the antenna architectures.

This work was partially completed while S. K. Shastri was interning at Mitsubishi Electric Research Laboratories.

<sup>1</sup>Available online at: <https://github.com/merlresearch/DeepBornFNO>

In this paper, we extend our previous operator learning framework, BFNO [14], to the case of realistic GPR acquisition and inversion. To this end, we consider the bistatic measurement setup that is commonly used in GPR surveys. We then present a modular framework that combines the BFNO module for wavefield propagation with a learned calibration network module that transforms wavefield measurements from a point-receiver configuration of the BFNO to measurements corresponding to a realistic GSSI-400 MHz receiver [20] located at the same position. The calibration network module can be adapted to other antenna architectures for which data is available. We demonstrate using extensive simulations on a synthetic dataset that our proposed framework can successfully recover the permittivity distribution of subsurface structures while remaining robust to measurement noise.

## II. PROPOSED METHOD

### A. Background

Considering the 2D scalar wave scenario with a homogeneous background, the Lippmann-Schwinger [5] integral equation fully characterizes the wave-object relationship:

$$u(\mathbf{x}) = u_{\text{in}}(\mathbf{x}) + k_b^2 \int_D g(\mathbf{x} - \mathbf{x}') f(\mathbf{x}') u(\mathbf{x}') d\mathbf{x}', \quad \forall \mathbf{x} \in \mathbb{R}^2 \quad (1)$$

where  $u(\mathbf{x})$  represents the total field,  $u_{\text{in}}(\mathbf{x})$  is the incident field,  $\epsilon_b$  is the background permittivity,  $k_b = \sqrt{\epsilon_b} \omega / c$  is the background wavenumber,  $c$  is the speed of light in vacuum,  $\omega$  is the angular frequency, and  $g$  is the Green's function for the background. Let  $\epsilon(\mathbf{x})$  denote the permittivity of the object. We assume that the permittivity contrast  $f(\mathbf{x}) = \epsilon(\mathbf{x}) / \epsilon_b - 1 = 0$  for  $\mathbf{x} \notin D$ , hence the integration domain can be confined to a bounded computational domain  $D \subset \mathbb{R}^2$ . Additionally, we assume that  $\epsilon$  and  $\epsilon_b$  are real-valued and frequency-independent, where  $\epsilon$  is used without the argument  $\mathbf{x}$  to refer to the permittivity distribution over all  $D$ . Denoting by  $\Gamma \subset \mathbb{R}^2$  is the set of receiver locations; the measurements then consist of the total field  $u(\mathbf{x})$ , where  $\mathbf{x} \in \Gamma$ .

A  $K^{\text{th}}$ -order IBA can be employed to estimate the total field using the following approximation:

$$u_{i+1}(\mathbf{x}) = u_{\text{in}}(\mathbf{x}) + k_b^2 \int_D g(\mathbf{x} - \mathbf{x}') f(\mathbf{x}') u_i(\mathbf{x}') d\mathbf{x}', \quad (2)$$

where  $u_0(\mathbf{x}) = 0$  and  $i = 1, \dots, K-1$ . In this approximation, the total field at the  $K^{\text{th}}$  iteration  $u_K(\mathbf{x})$  is used to compute the measurements by sampling the field at  $\mathbf{x} \in \Gamma$ .

### B. Forward Model

We propose to learn the forward model characterizing a GSSI-400 GPR setup directly from data due to the difficulty in devising an analytical forward model. We adopt a modular architecture where the first module behaves as a wave propagation operator and learns to predict the scattered wavefield  $\tilde{u}(\mathbf{x}) \triangleq u(\mathbf{x}) - u_{\text{in}}(\mathbf{x})$ , arising from a point-source incident upon an underground structure. The second module, referred to as the calibration network, learns to predict the GSSI-400 scattered wavefield measurements at the receiver location from

the predicted point-source scattered wavefield output by the first module. The objective of the first module closely aligns with the problem that we previously tackled in [14]. Drawing inspiration from both FNO [12] and IBA Eq. (2), Zhao et al. [14] introduced BFNO, a model adept at learning the wave propagation in a point source setup.

1) *Born FNO*: Consider a uniformly sampled 2D domain  $D \subset \mathbb{R}^2$  and sets  $\Omega \triangleq \{\omega_1, \omega_2, \dots, \omega_{N_\omega}\}$  and  $\mathcal{S} \triangleq \{1, 2, \dots, S\}$ . For all frequencies  $\omega \in \Omega$  and sources  $s \in \mathcal{S}$ , the BFNO is designed to predict the scattered wavefield  $\tilde{u}_s^\omega$  at each grid point in  $D$ . This is accomplished by considering the free-space incident wavefield  $\mathbf{u}_{\text{in},s}^\omega$  and the underground permittivity distribution  $\epsilon$ , both discretized on the same grid  $D$  of size  $n_1 \times n_2$ , as inputs. For our setup, the BFNO operator  $\mathcal{B}$  can be described as the mapping  $\mathcal{B}: \mathbb{R}^{n_1 \times n_2 \times 3} \rightarrow \mathbb{R}^{n_1 \times n_2 \times 2}$ , such that,  $\forall \mathbf{x} \in D$ ,  $\forall \omega \in \Omega$ , and  $\forall s \in \mathcal{S}$ :

$$v_\epsilon(\mathbf{x}) = P_\epsilon(\mathbf{x}, \epsilon(\mathbf{x})), \quad (3)$$

$$v_{0,s}^\omega(\mathbf{x}) = v_{\text{in},s}^\omega(\mathbf{x}) = P_{\text{in}}(\mathbf{x}, \text{Re}\{u_{\text{in},s}^\omega(\mathbf{x})\}, \text{Im}\{u_{\text{in},s}^\omega(\mathbf{x})\}), \quad (4)$$

$$v_{i+1,s}^\omega(\mathbf{x}) = v_{\text{in},s}^\omega(\mathbf{x}) + \sigma(W_1(\sigma(W_0(K(v_\epsilon, v_{i,s}^\omega)(\mathbf{x}))))), \quad (5)$$

$$K(v_\epsilon, v_{i,s}^\omega)(\mathbf{x}) = \mathcal{F}^{-1}(R \cdot \mathcal{F}(v_\epsilon v_{i,s}^\omega)(\mathbf{x})), \quad (6)$$

$$\tilde{u}_s^\omega(\mathbf{x}) = [\text{Re}\{u_s^\omega(\mathbf{x})\}, \text{Im}\{\tilde{u}_s^\omega(\mathbf{x})\}] = Q(v_{n,s}^\omega(\mathbf{x})), \quad (7)$$

where  $P_\epsilon$ ,  $P_{\text{in}}$ , and  $Q$  are local transformations parameterized by multi-layer perceptrons (MLPs),  $\mathcal{F}$  is the Fourier operator,  $n$  is the number of layers, and  $\sigma(\cdot)$  is the Leaky ReLU nonlinearity. We learn the BFNO model weights  $\phi_{\mathcal{B}}$  by training the model to minimize a normalized-mean-squared error:

$$\phi_{\mathcal{B}}^* = \underset{\phi_{\mathcal{B}}}{\text{argmin}} \sum_j \sum_\omega \sum_s \sum_{\mathbf{x} \in D_s^j} \frac{\|\tilde{u}_{\text{gt},s}^{\omega,j}(\mathbf{x}) - \mathcal{B}(\epsilon^j, \omega, s; \phi_{\mathcal{B}})(\mathbf{x})\|_2}{\|\tilde{u}_{\text{gt},s}^{\omega,j}(\mathbf{x})\|_2}, \quad (8)$$

where  $\epsilon^j$  is a permittivity distribution from the training sample  $j$ ,  $\tilde{u}_{\text{gt},s}^{\omega,j}$  is the ground truth scattered field of source  $s$  for  $\epsilon^j$  at frequency  $\omega$ , and  $D_s^j \subseteq D$  is the random subset of gridpoints of the full domain  $D$  used for training sample  $j$  and source  $s$ .

2) *Calibration Module*: In the second phase of forward modeling, we aim to transform the predicted point-source scattered wavefield measurements from the BFNO to GSSI-400 scattered wavefield measurements. We denote this phase as the calibration module. In this context, we investigate two distinct calibration models to establish this mapping: one is a linear model, and the other is a non-linear model. In the nonlinear case, we use a neural network  $\Lambda$  with parameters  $\lambda_c$  that are determined by minimizing the following loss function:

$$\lambda_c^* = \underset{\lambda_c}{\text{argmin}} \sum_i \sum_s \|\mathbf{y}_s^i - \Lambda(\tilde{\mathbf{y}}_s^i)\|_2^2, \quad (9)$$

where  $\tilde{\mathbf{y}}_s^i$  and  $\mathbf{y}_s^i$  represent vectors whose entries contain the point-source and GSSI-400 scattered wavefield measurements at all frequencies, respectively, for a given training sample  $i$  and source  $s \in \mathcal{S}$ . In the linear case,  $\Lambda$  is an affine transformation operator.

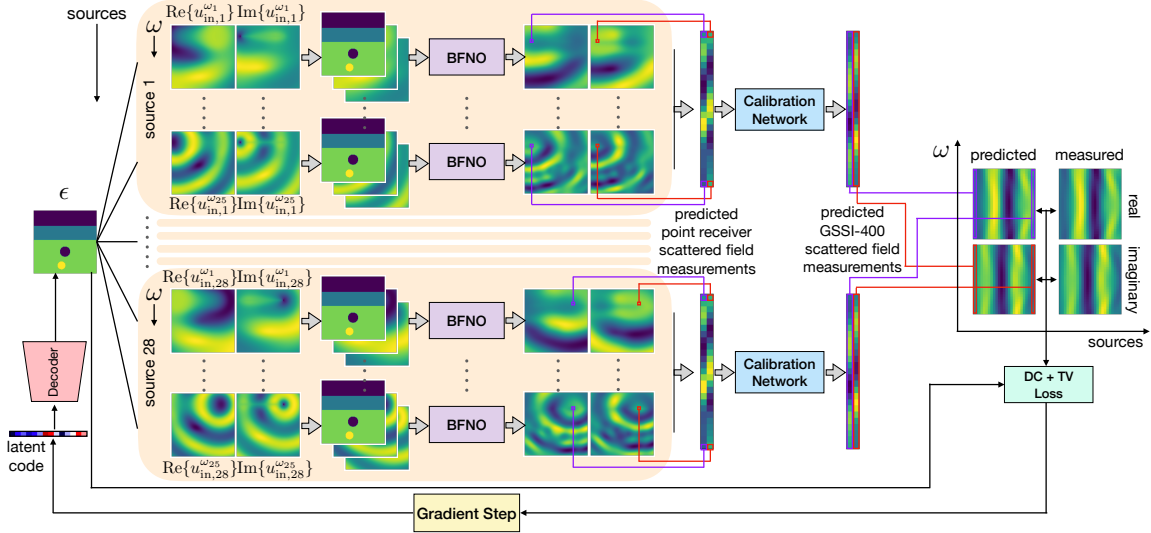


Fig. 1. The figure illustrates the algorithm pipeline, where the BFNO, Decoder (prior model), and Calibration Networks are pre-trained. During testing, the decoder maps a latent code  $\mathbf{z}$  to the estimated permittivity distribution  $\epsilon$ . Subsequently,  $\epsilon$  and the incident wavefield for each source and frequency are used by the BFNO to predict the corresponding point-source scattered wavefield. The point-source scattered wavefield at the measurement locations is then transformed into the corresponding GSSI-400 scatter wavefield using the calibration network. These predictions are used to compute the data consistency (DC) loss with respect to the noisy GSSI-400 measurements. The latent code is optimized using the ADAM optimizer to minimize the DC loss for all sensors and frequencies, along with the total variation (TV) loss of the estimated subsurface permittivity distribution.

### C. Learned Signal Prior

Given the highly ill-posed nature of the problem arising from sparse and restricted angle measurements, we constrain the solution space to a low-dimensional subspace known as the latent space, encoded by a convolutional auto-encoder  $\mathcal{E}$ . Our objective is to recover the latent code, which, when decoded using a decoder  $\mathcal{G}$ , recovers the permittivity distribution  $\epsilon$ . The autoencoder weights are computed by minimizing the following loss function:

$$(\phi_{\mathcal{G}}^*, \phi_{\mathcal{E}}^*) = \underset{\phi_{\mathcal{G}}, \phi_{\mathcal{E}}}{\operatorname{argmin}} \sum_i \|\mathcal{G}(\mathcal{E}(\epsilon^i; \phi_{\mathcal{E}}); \phi_{\mathcal{G}}) - \epsilon^i\|_2^2 + \frac{1}{\sigma_{\mathcal{E}}^2} \|\mathcal{E}(\epsilon^i; \phi_{\mathcal{E}})\|_2^2, \quad (10)$$

where  $\epsilon^i$  is the permittivity distribution at the training sample  $i$ , and  $\sigma_{\mathcal{E}}$  is a fixed scalar.

### D. Inverse Problem

The permittivity reconstruction problem can now be posed as finding the latent code  $\hat{\mathbf{z}}$  that minimizes the following reconstruction objective:

$$\hat{\mathbf{z}} = \underset{\mathbf{z}}{\operatorname{argmin}} \sum_s \left\| \begin{bmatrix} y_s^{\omega_1} \\ \vdots \\ y_s^{\omega_{N_\omega}} \end{bmatrix} - \Lambda \left( \begin{bmatrix} H_s(\mathcal{B}(\mathcal{G}(\mathbf{z}), \omega_1, s)) \\ \vdots \\ H_s(\mathcal{B}(\mathcal{G}(\mathbf{z}), \omega_{N_\omega}, s)) \end{bmatrix} \right) \right\|_2^2 + \mathcal{R}(\mathcal{G}(\mathbf{z})), \quad (11)$$

where  $H_s$  is a sampling operator that selects the wavefield at the receiver location for each of the sensor  $s \in \mathcal{S}$ ,  $y_s^\omega$  is the noisy GSSI-400 scattered field measurement at frequency  $\omega \in \Omega$  for source  $s \in \mathcal{S}$ , and  $\mathcal{R}(\cdot)$  represents a suitable regularizer such as total variation. The unknown permittivity distribution of the underground scene is then recovered as  $\hat{\epsilon} = \mathcal{G}(\hat{\mathbf{z}})$ . An overview of our approach is illustrated in Fig. 1.

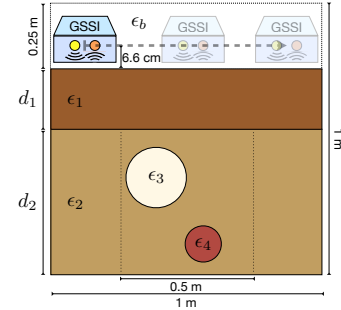


Fig. 2. Example gprMax setup and the underground scene considered in this work. The GSSI-400 scanner moves horizontally to collect measurements.

## III. NUMERICAL EXPERIMENTS

### A. Dataset

Our dataset encompasses gprMax [20, 21] simulations of 400 underground scenes, split between 390 training scenes to train the BFNO module and 10 test scenes reserved for solving the inverse problem. Of the 390 scenes, 190 are used to train the calibration module. Furthermore, we generated an additional 5,000 underground scenes to train the encoder  $\mathcal{E}$  and decoder  $\mathcal{G}$ . Both point source (Ricker wavelet within [250MHz, 700MHz] band) and GSSI-400 measurements are generated for training and testing.

The underground scenes are of size  $1\text{m} \times 1\text{m}$  discretized at  $157 \times 157$  (i.e.  $n_1 = n_2 = 157$ ) pixel grid and composed of three horizontal layers, as illustrated in Fig. 2. The top layer comprises 0.25 m of air with  $\epsilon_b = 1$  and serves as the placement for the GSSI-400, point-source, and point-receiver components. The depth and permittivity of the second layer are randomly sampled from  $d_1 \sim \mathcal{U}(0.15, 0.3)$  m and  $\epsilon_1 \sim \mathcal{U}(3, 5)$ , respectively. The depth of the third layer is  $d_2 = 1\text{m} - 0.25\text{m} - d_1$ , and  $\epsilon_2 \sim \mathcal{U}(5, 10)$ . The third layer contains two non-overlapping objects, each positioned randomly within the central  $0.5\text{m} \times d_2$  area. The first object is a circle with a radius sampled

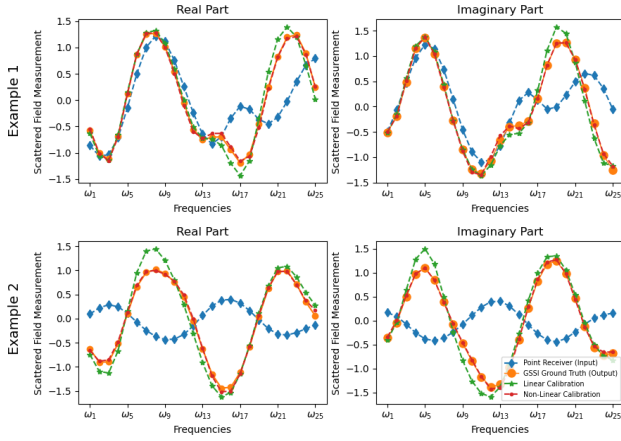


Fig. 3. Example predictions of GSSI-400 scattered field measurements.

from  $\mathcal{U}(0.05, 0.1)$  m, and it is composed of air; therefore,  $\epsilon_3=1$ . The second object is either a circle, with a radius randomly sampled from  $\mathcal{U}(0.05, 0.1)$  m, or a square, with a side randomly sampled from  $\mathcal{U}(0.05, 0.1)$  m. The permittivity of the second object is randomly sampled from  $\epsilon_4 \sim \mathcal{U}(3, 10)$ . To expedite the grMax simulation and data collection, we sample a subset  $D_s^j$  comprising 20% of the point receiver locations from the  $157 \times 157$  grid for a given source  $s$  and underground scene  $j$ .

### B. Training Details

1) *Born FNO*: We used a single 5-layer BFNO similar to [14] that predicts the point-source scattered wavefield for a given point-source location, frequency, and permittivity distribution of the underground scene. The BFNO model was trained with the loss function Eq. (8), a mini-batch size of 64, over 100,000 steps, utilizing the Adam optimizer. The learning rate started at  $10^{-3}$  and reduced by a factor of 2 at every 20,000 steps.

2) *Calibration Network*: We learn two calibration networks: one an affine transformation, and the other a non-linear deep network composed of an MLP with 4 hidden layers and a *tanh* activation function. Both networks were trained with  $\ell_2$  loss function between the input point source  $\tilde{\mathbf{y}}_s \in \mathbb{C}^{25 \times 1}$  measurements and output GSSI-400  $\mathbf{y}_s \in \mathbb{C}^{25 \times 1}$  measurements. Both these networks were trained with  $\ell_2$  loss function, a mini-batch size of 128, over 42,000 steps, utilizing the Adam optimizer. The learning rate started at  $10^{-3}$  and reduced by a factor of 2 at 21,000 steps.

Fig. 3 illustrates the predictions of the GSSI-400 scattered wavefield measurements made by the calibration techniques for two different test cases. The mean squared error (MSE) averaged over all the test cases for the linear calibration is 0.0302, while for the non-linear calibration, it is 0.0023.

3) *Auto-Encoder*: We train a convolutional autoencoder model to impose a prior on the underground scenes. The encoder employs a sequence of 5 convolutional layers with batch normalization and LeakyReLU activation functions to extract hierarchical features from the input underground permittivity

TABLE I  
QUANTITATIVE PERFORMANCE COMPARISON OF VARIOUS RECEIVER AND CALIBRATION SETUPS WITH NOISELESS MEASUREMENTS.

Receiver	Fidelity	Calibration	PSNR	RSNR	SSIM
Point	Non-Realistic	-	21.23	17.35	0.9094
GSSI-400	Realistic	Linear	14.44	10.55	0.7254
GSSI-400	Realistic	Non-Linear	19.29	15.41	0.8782

TABLE II  
QUANTITATIVE PERFORMANCE AT VARIOUS MEASUREMENT SNRS.

Measurement SNR	PSNR	RSNR	SSIM
15 dB	18.12	14.23	0.8494
20 dB	18.71	14.83	0.8693
25 dB	19.21	15.32	0.8706

distribution. The latent representation, sized  $64 \times 1$ , is obtained by flattening the output of the last convolutional layer of the encoder and passing it through a fully connected layer. The decoder network mirrors the encoder's structure in reverse order, gradually upsampling the latent space to generate the output permittivity distribution. The autoencoder was trained with the loss function Eq. (10) with  $\sigma_\epsilon=10^{-3}$ , a mini-batch size of 2,048, over 25,000 steps, utilizing the Adam optimizer. The learning rate started at  $10^{-3}$  and reduced by a factor of 2 at every 5,000 steps.

### C. Reconstruction Algorithm Implementation Details

In our setup,  $S=28$  and  $N_\omega=25$ . For regularization  $\mathcal{R}(\cdot)$ , we use an isotropic total variation function. We use ADAM [22] optimizer for 550 iterations to solve the optimization problem Eq. (11). For each test case, we experiment with initial learning rates of 0.005, 0.01, and 0.015. We then report the reconstruction that results in the lowest optimization loss in Eq. (11). We reduce the learning rate by a factor of 2 for the last 50 iterations of the algorithm. Additionally, we integrate the incremental frequency framework [10] into the optimization process. Similar to [14], we fine-tune our prior  $\mathcal{G}$  by jointly optimizing for  $\mathbf{z}$  and  $\phi_G$ , starting at iteration 350.

### D. Reconstruction Results

Table I shows the average peak signal-to-noise ratio (PSNR), reconstruction SNR (RSNR), and structural similarity (SSIM) index performance for the various scenarios. The first row in the table corresponds to the reconstruction that assumes knowledge of the point-receiver, thereby eliminating the need for the calibration process. This point-receiver setup is not practical but serves as an upper bound on what one could expect from an optimally calibrated GSSI-400 setup. The table shows the non-linear calibration setup outperforms the linear calibration, with its performance only slightly trailing behind the non-realistic point-receiver setup.

Table II presents the averaged performance metrics for the reconstruction obtained using non-linear calibration across the test cases at various measurement SNRs. Additive white Gaussian noise is used to simulate noisy measurements. Observing the table, it is evident that the algorithm demonstrates

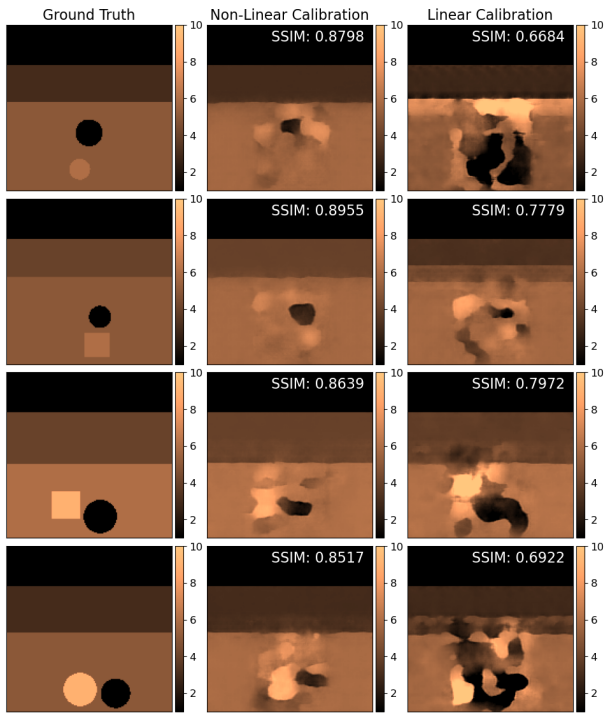


Fig. 4. Example permittivity distribution reconstructions for non-linear and linear calibration setups at 20 dB measurement SNR.

robustness to noise in the system. We further illustrate example reconstructions for both non-linear and linear calibration setups at a measurement SNR of 20 dB in Fig. 4. The figure suggests that the reconstruction algorithm employing non-linear calibration accurately recovers the depths and permittivity values of all layers and objects, outperforming the linear calibration setup.

#### IV. CONCLUSION

We considered the problem of reconstructing subsurface permittivity distribution from realistic GPR measurements. The forward model of our proposed framework first uses a BFNO model to learn the complicated wave-object interaction, predicting the scattered wavefield measurements of a point receiver. Subsequently, a deep calibration network maps these measurements to the desired response of a receiving antenna architecture. This learned forward model, combined with a learned prior, is then utilized in an optimization algorithm to recover the permittivity distribution. Through numerical experiments on simulated GSSI-400 antenna measurements, we demonstrate that the proposed framework, with a non-linear calibration network, enables accurate reconstruction of permittivity distribution even in the presence of measurement noise, significantly outperforming its linear-calibration counterpart.

#### ACKNOWLEDGMENT

The authors would like to thank Prof. Philip Schniter for providing computing resources to complete part of the simulations performed in this work.

#### REFERENCES

- [1] S. Lee, G. A. McMechan, and C. L. Aiken, "Phase-field imaging: The electromagnetic equivalent of seismic migration," *Geophysics*, vol. 52, no. 5, pp. 678–693, 1987.
- [2] A. J. Witten, J. E. Molyneux, and J. E. Nyquist, "Ground penetrating radar tomography: algorithms and case studies," *IEEE Transactions on Geoscience and Remote Sensing*, vol. 32, no. 2, pp. 461–467, 1994.
- [3] R. Persico, *Introduction to ground penetrating radar: inverse scattering and data processing*, John Wiley & Sons, 2014.
- [4] Emil W., "Three-dimensional structure determination of semi-transparent objects from holographic data," *Optics Communications*, vol. 1, no. 4, pp. 153–156, 1969.
- [5] B. A. Lippmann and J. Schwinger, "Variational principles for scattering processes. i," *Physical Review*, vol. 79, no. 3, pp. 469, 1950.
- [6] Y. Ma, H. Mansour, D. Liu, P. T. Boufounos, and U. S. Kamilov, "Accelerated image reconstruction for nonlinear diffractive imaging," in *IEEE International Conference on Acoustics, Speech and Signal Processing*, 2018, pp. 6473–6477.
- [7] T. Pham, E. Soubies, A. Ayoub, J. Lim, D. Psaltis, and M. Unser, "Three-dimensional optical diffraction tomography with lippmann-schwinger model," *IEEE Transactions on Computational Imaging*, vol. 6, pp. 727–738, 2020.
- [8] L. Song and Q. H. Liu, "Ground-penetrating radar land mine imaging: Two-dimensional seismic migration and three-dimensional inverse scattering in layered media," *Radio science*, vol. 40, no. 1, pp. 1–15, 2005.
- [9] E. Soubies, T. Pham, and M. Unser, "Efficient inversion of multiple-scattering model for optical diffraction tomography," *Opt. Express*, vol. 25, no. 18, pp. 21786–21800, Sep 2017.
- [10] A. Kadu, H. Mansour, and P. T. Boufounos, "High-contrast reflection tomography with total-variation constraints," *IEEE Transactions on Computational Imaging*, vol. 6, pp. 1523–1536, 2020.
- [11] M. Born and E. Wolf, *Principles of optics: electromagnetic theory of propagation, interference, and diffraction of light*, Elsevier, 2013.
- [12] Z. Li, N. Kovachki, K. Azizzadenesheli, B. Liu, K. Bhattacharya, A. Stuart, and A. Anandkumar, "Fourier neural operator for parametric partial differential equations," 2020.
- [13] Y. Yang, A. F. Gao, J. C. Castellanos, Z. E. Ross, K. Azizzadenesheli, and R. W. Clayton, "Seismic wave propagation and inversion with neural operators," 2021.
- [14] Q. Zhao, Y. Ma, P. Boufounos, S. Nabi, and H. Mansour, "Deep born operator learning for reflection tomographic imaging," in *IEEE International Conference on Acoustics, Speech and Signal Processing (ICASSP)*, 2023, pp. 1–5.
- [15] S. Lambot, E. C. Slob, I. van den Bosch, B. Stockbroeckx, and M. Vanclooster, "Modeling of ground-penetrating radar for accurate characterization of subsurface electric properties," *IEEE Transactions on Geoscience and Remote Sensing*, vol. 42, no. 11, pp. 2555–2568, 2004.
- [16] T. Forbriger, L. Groos, and M. Schäfer, "Line-source simulation for shallow-seismic data. part 1: Theoretical background," *Geophysical Journal International*, vol. 198, no. 3, pp. 1387–1404, 2014.
- [17] M. Schäfer, L. Groos, T. Forbriger, and T. Bohlen, "Line-source simulation for shallow-seismic data. part 2: Full-waveform inversion—a synthetic 2-d case study," *Geophysical Journal International*, vol. 198, no. 3, pp. 1405–1418, 2014.
- [18] L. Sirgue, O. I. Barkved, J. A. Dellinger, J. Etgen, U. K. Albertin, and J. H. Kommedal, "Thematic set: Full waveform inversion: the next leap forward in imaging at valhall," *First Break*, vol. 28, pp. 65–70, 2010.
- [19] J. Virieux and S. Operto, "An overview of full-waveform inversion in exploration geophysics," *GEOPHYSICS*, vol. 74, no. 6, pp. WCC1–WCC26, 2009.
- [20] S. Stadler and J. Igel, "A numerical study on using guided gpr waves along metallic cylinders in boreholes for permittivity sounding," in *2018 17th International Conference on Ground Penetrating Radar (GPR)*, 2018, pp. 1–4.
- [21] C. Warren, A. Giannopoulos, and I. Giannakis, "gprmax: Open source software to simulate electromagnetic wave propagation for ground penetrating radar," *Computer Physics Communications*, vol. 209, pp. 163–170, 2016.
- [22] D. P. Kingma and J. Ba, "Adam: A method for stochastic optimization," *arXiv preprint arXiv:1412.6980*, 2014.